AGU PUBLICATIONS

JGR

Journal of Geophysical Research: Solid Earth

RESEARCH ARTICLE
10.1002/2015JB012392

Key Points:
- D″ discontinuity height ranges from 180 to 380 km
- Double Scd arrivals consistent with rapid topographic relief
- Lack of Scd arrivals may indicate a hole in the discontinuity

Supporting Information:
- Figures S1–S23 and Table S1

Correspondence to:
M. S. Thorne,
michael.thorne@utah.edu

Citation:
Whittaker, S., M. S. Thorne, N. C. Schmerr, and L. Miyagi (2015), Seismic array constraints on the *D*″ discontinuity beneath Central America, *J. Geophys. Res. Solid Earth*, *120*, doi:10.1002/2015JB012392.

Received 28 JUL 2015
Accepted 1 DEC 2015
Accepted article online 7 DEC 2015

Seismic array constraints on the *D*″ discontinuity beneath Central America

Stefanie Whittaker[1], Michael S. Thorne[2], Nicholas C. Schmerr[3], and Lowell Miyagi[2]

[1]Department of Geosciences, University of Alaska Fairbanks, Fairbanks, Alaska, USA, [2]Department of Geology and Geophysics, University of Utah, Salt Lake City, Utah, USA, [3]Department of Geology, University of Maryland, College Park, Maryland, USA

Abstract We analyzed 16,150 transverse component seismic recordings from 54 deep-focus earthquakes in the South American and Caribbean regions recorded at broadband stations in North America between 2005 and 2012. We treated subgroups of seismic stations within 3° radius geographical bins as seismic arrays and performed vespagram analysis. We focused on the *S*, *ScS*, and *Scd* arrivals and collected data in the epicentral distance range from 55° to 90°. In particular, we searched for *D*″ discontinuity presence in the vespagrams in a 25° by 35° (or 1520 by 2130 km) area beneath Central America. Analysis of these data showed 125 clear *Scd* observations, 180 *Scd* observations of lesser quality, and 343 nonobservations. We produced a new map of the discontinuity height beneath Central America. Our map shows an average discontinuity height of 286 ± 6 km ($\sigma = 76$ km). The region is punctuated by a large topographic high centered at approximately 10°N and 90°W with a maximum height of 380 km. Two smaller topographic highs are located at approximately 4°N and 81°W (discontinuity height of 320 km) and at 4°N and 70°W (height of 315 km). The observation of multiple *Scd* arrivals collocated with the strongest gradients in inferred topography provides evidence for topographic variation on the discontinuity rather than multiple discontinuities. The regions where the discontinuity has the greatest height can be explained by localized enrichment of mid-ocean ridge basalt from the subducted Farallon slab impinging on the core-mantle boundary.

1. Introduction

The *D*″ discontinuity was first observed a little over three decades ago as a triplication of the *SH* wave field beneath Central America [*Lay and Helmberger*, 1983a, 1983b]. In the ensuing decades multiple observations of the discontinuity have been reported using a variety of seismic phase arrivals (see reviews [*Lay and Garnero*, 2011; *Wysession et al*., 1998]). The majority of observations are reported above regions that show faster than average lower mantle seismic wave speeds in global tomographic models. For example, the discontinuity is readily apparent beneath Alaska [e.g., *Vidale and Benz*, 1993; *Young and Lay*, 1990], Central America (see *Kito et al*. [2007] and *Thomas et al*. [2004] for a summary of observations), Siberia [e.g., *Houard and Nataf*, 1992; *Weber and Davis*, 1990], and Central Asia [e.g., *Gaherty and Lay*, 1992; *Kendall and Shearer*, 1994]. Observations of the discontinuity beneath seismically slower than average regions in the lowermost mantle have been primarily confined to the central Pacific region [e.g., *Avants et al*., 2006; *Garnero et al*., 1993]. From these observations the *D*″ discontinuity has been characterized as ranging in height from roughly 100 to 430 km, with *S* wave velocity increases (δV_S) from 2.0 to 4.0% and *P* wave velocity (δV_P) changes from −3.0 to 3.0% across the discontinuity [*Cobden and Thomas*, 2013].

The origin of the rapid increase in *S* wave velocity giving rise to the *D*″ discontinuity has intrigued researchers for decades. The discovery of a phase transition from bridgmanite to postperovskite (ppv) [*Murakami et al*., 2004; *Oganov and Ono*, 2004; *Shim et al*., 2004] at pressures and temperatures where the *D*″ discontinuity is seismically observed has provided a plausible explanation for the existence of the discontinuity. However, much uncertainty still exists on the nature of a possible phase transition, especially when considering the effects of variations in mineralogy and composition believed to be present in the deepest mantle [*Grocholski et al*., 2012; *Zhang et al*., 2014].

The *D*″ discontinuity beneath the Central American region has received particular attention due to excellent ray path coverage from deep South American events recorded in North America, revealing a complex set of observations. Past observations in this region have demonstrated a discontinuity height ranging from 140 to

370 km above the core-mantle boundary (CMB) with a δV_S increase of 1.0 to 3.0% and a δV_P change of −3.0 to 1.0% [*Cobden and Thomas*, 2013; *Kito et al*., 2007; *Thomas et al*., 2004]. Extensive lateral variation in D″ discontinuity height has been inferred across the region. For example, near 90°W and 5°N a roughly 150 km step in topography has been identified in multiple studies [*Hutko et al*., 2006; *Kito et al*., 2007; *Thomas et al*., 2004; *van der Hilst et al*., 2007]. The origin of this step in topography is unknown, yet speculation centers on the subducted Farallon slab folding over on itself as it impinges on the CMB. Nevertheless, discontinuity topography trades off with seismic velocity and two studies have modeled the discontinuity in this region as potentially flat lying and underlain with lateral *S* wave velocity perturbations [*Lay et al*., 2004; *Thorne et al*., 2007]. Furthermore, the discontinuity at this location appears exceptionally sharp and is consistent with the transition occurring over a depth range of less than 30 km [*Lay*, 2008]. A second, negative impedance contrast with increasing depth has also been detected near 90°W and 5°N at roughly 200 km above the CMB [*Kito et al*., 2007; *Thomas et al*., 2004]. A negative impedance reflector at a maximum height of 150 km above the CMB is also observed by *van der Hilst et al*. [2007]. In this study, the negative impedance reflector appears to have a concave up shape and is too thin to be detected directly beneath the Central American region but is apparent to the far eastern and western edges of the Central American region. Expanding on the study of *van der Hilst et al*. [2007], *Shang et al*. [2014] image a negative impedance reflector at roughly 200 km above the CMB consistently across the entire Central American region. Using a waveform inversion approach, *Kawai et al*. [2007] also infer a decrease in *S* wave velocities at a height of roughly 100 km above the CMB. Additional intermittent reflectors of unknown impedance polarity have been detected between roughly 50 and 100 km beneath the D″ discontinuity [*van der Hilst et al*., 2007] and at about 150 km above the *D*″ discontinuity [*Shang et al*., 2014].

In addition to discontinuity topography and multiple reflectors, observations of the *D*″ discontinuity have also been associated with observations of lower mantle anisotropy [e.g., *Matzel et al*., 1996]. The region beneath Central America has been characterized with vertical transverse isotropy (VTI), the magnitude of which may correlate with inferred discontinuity height [*Rokosky et al*., 2004]. Nonetheless, the region displays complex anisotropic behavior which is difficult to explain solely with VTI [*Maupin et al*., 2005].

The first studies of the *D*″ discontinuity looked for the *S* wave triplication within individual waveforms. Some of these earliest efforts utilized seismic array processing methods in order to boost the signal-to-noise ratio of low-amplitude arrivals associated with the discontinuity [e.g., *Krüger et al*., 1993; *Weber*, 1993; *Weber and Davis*, 1990; *Yamada and Nakanishi*, 1998]. Many recent efforts have used increasingly sophisticated methods to detect the discontinuity including, 3-D grid migration and double-array stacking [*Kito et al*., 2007], Kirchhoff migration [*Hutko et al*., 2006], full waveform inversion [*Kawai and Geller*, 2010], and the generalized radon transform technique [*Ma et al*., 2007; *Shang et al*., 2014; *van der Hilst et al*., 2007; *Wang et al*., 2008, 2006]. Array processing approaches continue to be utilized [e.g., *Chaloner et al*., 2009; *Cobden and Thomas*, 2013] and one recent effort has applied array processing techniques to noise correlograms to image the discontinuity [*Poli et al*., 2015].

In this study, we utilize three-component broadband data recorded in North America from events in South and Central America, taking advantage of the vast number of seismic stations made available through the Earthscope transportable array (TA) and flexible array (FA) experiments and additions to the Advanced National Seismic System backbone array. The large number and high density of available stations make it possible to examine the *D*″ discontinuity beneath Central America treating subgroups of stations as seismic arrays and thus allow us to implement array processing techniques on these three-component recordings. Here we expand the range of available data that can be used to image the *D*″ discontinuity through waveform modeling techniques and present a new map of discontinuity height.

2. Data

In this study, we use the seismic phase *Scd* to investigate the *D*″ discontinuity beneath Central America. *Scd* is a part of the triplication that occurs as the downgoing *S* wave refracts beneath the *D*″ discontinuity. Ray paths for the direct *S*, *Scd*, and *ScS* arrivals are shown in Figure 1a and example waveforms are shown in Figure 1b for a 500 km deep event. Here we have aligned transverse component, displacement synthetic seismograms on the direct *S* arrival. The *Scd* arrival is apparent between the direct *S* and *ScS* arrivals for epicentral distances between roughly 68° and 83°. For distances less than 68° the *Scd* arrival is low amplitude and difficult to

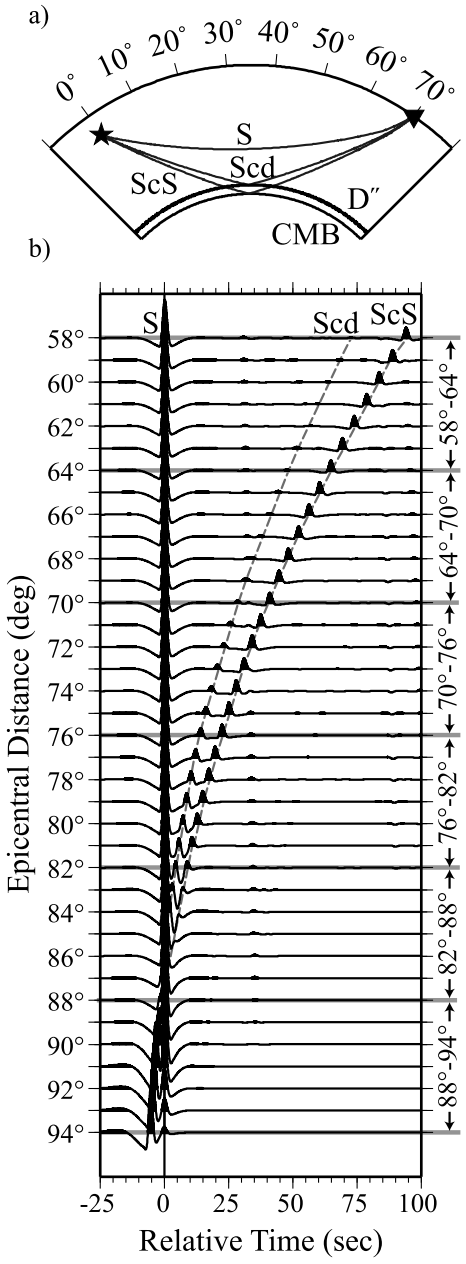

Figure 1. (a) Ray paths of seismic phases used in this study. The star and the inverted triangle represent the event epicenter at 500 km depth and the recording station located at a great-circle arc distance of 70°, respectively. The *S*, *Scd*, and *ScS* seismic phases are labeled. (b) Synthetic seismograms of the transverse component displacement aligned in time on the direct *S* wave arrival are shown. The observed phases are labeled. Here we used a *D″* discontinuity height of 200 km, an *S* wave velocity increase of 2.0%, and a 0% change in density to compute these synthetics. Distance labels along the right edge of the plot are discussed in section 3.2.

observe in individual traces. At distances approximately greater than 83° the *Scd* arrival passes through and ultimately arrives ahead of the direct *S* wave arrival. This is not commonly observed in real data [e.g., *Young and Lay*, 1987] but has been noted in some efforts [e.g., *He and Wen*, 2012]. The reflected arrival, *Sbc*, is a low-amplitude, negative polarity arrival that can be seen by careful inspection of these synthetic seismograms in the shoulder of *Scd* and is also not typically observed in data.

We collected broadband data for all South and Central American events occurring between May 2005 and May 2012 with depths $\geq$75 km, moment magnitudes (M_W) between 5.4 and 6.8, and within the epicentral distance range $55° \leq \Delta \leq 90°$ at all recording stations in the continental United States. We chose this time frame to take advantage of data availability from both flexible array (FA) and transportable array (TA) components of the Earthscope program. Our initial data set included waveforms for 58 events, totaling 25,139 individual records. The data processing steps were as follows: (1) removal of the instrument response and integrating the velocity seismograms to displacement, (2) rotation of the seismograms to radial and transverse components, and (3) band-pass filtering these data with corners between 1 and 20 s. We selected this narrow filter band because in later processing steps (see section 3.2) we calculate vespagrams, and the long period energy is especially problematic in the vespa process. We visually inspected each record for clear *S* and *ScS* arrivals. If both the *S* and *ScS* arrivals were not readily distinguishable on the transverse component recordings, we discarded it. We manually picked the maximum amplitude of the *S* arrival and aligned our data on the peak, normalizing the peak amplitude to unity. Our final data set is composed of 53 South American events and one deep Caribbean event. After the quality control steps outlined above, we retained recordings for 16,150 station-event pairs.

Table S1 in the supporting information summarizes the events used in this study, and Figure 2 shows our final data set of 54 events (red stars), all broadband stations used (blue inverted triangles), and the CMB bounce points of *ScS* for each event-station pair. The CMB bounce points span a distance range of roughly 25° by 35° (or 1520 by 2130 km) along the CMB.

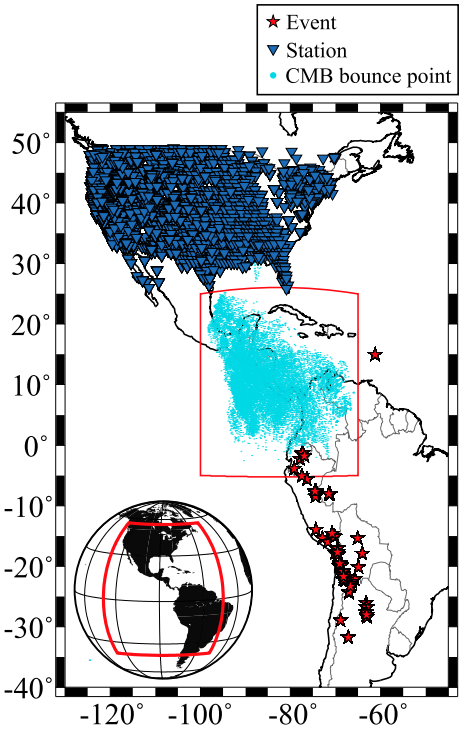

Figure 2. Events (red stars) and stations (blue triangles) used in this study. The light blue dots show the *ScS* bounce points on the CMB. The red box outlining the CMB bounce points around Central America and northern South America is our focus study area shown in later plots.

3. Methods

Our data analysis consists of grouping stations recording each event into geographical bins and treating each station grouping as a seismic array. We then use vespagram processing [e.g., *Rost and Thomas*, 2009] on each array and search for detections of the *Scd* arrival in the vespagrams. When the *Scd* phase is detected, we measure the differential travel times: *ScS-Scd* ($\delta T_{ScS\text{-}Scd}$) and *Scd-S* ($\delta T_{Scd\text{-}S}$), the differential amplitudes: *Scd/S* ($\delta A_{Scd/S}$) and *ScS/S* ($\delta A_{ScS/S}$), and differential slownesses: *Scd-S* ($\delta u_{Scd\text{-}S}$) and *ScS-Scd* ($\delta u_{ScS\text{-}Scd}$). These measurements are compared to synthetic seismogram predictions, and we estimate the height of the *D″* discontinuity. Sections 3.1 and 3.2 outline the methods by which we compute synthetic seismograms and how we use these predictions to arrive at height estimates. Section 3.3 describes how we group our data into geographic bins and our criteria for denoting a positive *Scd* observation. These observations are used to estimate the *D″* discontinuity height above the CMB.

3.1. Synthetic Seismograms

We compare our data to synthetic seismograms generated using the SHaxi method [*Jahnke et al.*, 2008]. The SHaxi method has been used in previous studies of *D″* discontinuity structure [*Lay et al.*, 2006; *Thorne et al.*, 2007; *Yao et al.*, 2015] and allows for computation of two-dimensional (2-D) *D″* discontinuity structure as may be encountered in our study region [*Hutko et al.*, 2006; *Shang et al.*, 2014; *Sun et al.*, 2006; *Thomas et al.*, 2004; *Wang et al.*, 2008]. The SHaxi method is a 2.5-D finite difference technique whereby a model generated on a 2-D grid is rotated around a symmetry axis joining the earthquake source to the center of the Earth. Hence, computation is performed on a 2-D grid, yet 3-D geometric spreading is retained. Our computations use 30,000 grid points in the lateral direction (angular distances from 0° to 180°) and 5200 grid points in the radial direction (from the surface to the CMB). We filter our synthetic seismograms by convolution with a 5 s dominant period Gaussian wavelet. Seismograms are calculated for epicentral distances between 55° and 95° with 0.1° spacing between receivers.

We first computed synthetic seismograms for 1-D *D″* discontinuity models where we varied two parameters: (1) height (*h*) above the CMB and (2) δV_S relative to the preliminary reference Earth model (PREM) [*Dziewonski and Anderson*, 1981]. Our primary database consisted of models where the event depth was fixed at 500 km. We allowed the *D″* discontinuity height to vary from 50 to 500 km in 50 km intervals, and we allowed δV_S to vary from +0.5 to +3.0% in 0.5% increments. Thus, we generated models for 10 unique heights and 6 unique *S* wave velocity increases for a total of 60 models. We also computed synthetics where we fixed δV_S at 2.0% for each *D″* discontinuity height outlined above and for event depths ranging from 100 to 600 km in 100 km intervals. These synthetics are compared with data to estimate *D″* discontinuity height.

3.2. *D″* Discontinuity Height Estimates

As the *Scd* phase is typically a low-amplitude arrival, we used fourth root vespagrams to increase our detection ability. The vespagram is calculated by shifting the times of seismograms within the array with respect to the array centroid for arrivals with different apparent slownesses and with a constant back azimuth. The shifted seismograms are then stacked (fourth root) to form a beam. The energy in the beam is plotted as arrival time versus slowness. This processing causes the incoherent signal amplitude to decrease and the coherent signal amplitude to increase. Although the waveforms become distorted, we still are able to obtain measurements of slowness, travel time, and relative amplitude [*Rost and Thomas*, 2009].

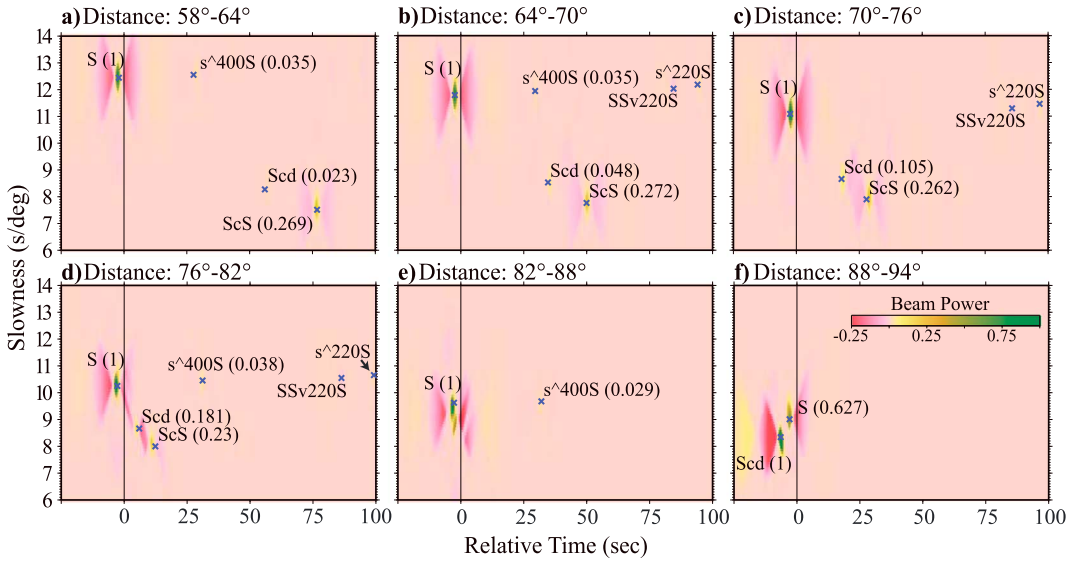

Figure 3. Plots of fourth root vespagrams from SHaxi synthetic seismograms. Plots are made for a *D″* discontinuity height of 200 km and δV_S of 2%. Each panel shows the vespagram calculated for data sorted into 6° epicentral distance intervals. For example, Figure 3a shows the vespagram for synthetics in the distance range from 58° to 64°. A blue cross is drawn at the peak time and slowness of each arrival for the seismic phases *S*, *ScS*, *Scd*, *s^400S*, *SSv220s*, and *s^220S* (phase labels are named by the convention used in the TauP toolkit [*Crotwell et al.*, 1999]). The beam amplitude for *S*, *ScS*, and *Scd* are located within the brackets and normalized to unity on the direct *S* arrival.

Vespagrams for a model with event depth of 500 km, *D″* discontinuity height of 200 km, no density change, and a velocity increase of 2.0% are shown in Figure 3. These vespagrams are computed from synthetics gathered into 6° epicentral distance bins with 3° of overlap. In Figure 3 we show six of the bins with no overlap. For example, Figure 3a shows vespagrams computed for synthetic seismograms in the distance range of 58°–64°. For comparison, synthetic waveforms for these vespagrams are shown in Figure 1b (the distance range of each of the six vespagrams shown in Figure 3 is labeled along the right side of Figure 1b). The vespagrams are aligned in time relative to the direct *S* wave and are normalized in amplitude (beam power) by the largest arrival in each vespagram. In Figure 3a the direct *S* wave has an amplitude of 1 (amplitude is shown in parentheses next to the arrival). The negative polarity (magenta) sidelobes are due to the narrow band filter. We processed our synthetic seismograms identically to the methods used to process data as explained previously. The *Scd* phase shows up clearly in Figures 3b–3d at great-circle arc distances of 64° to 82°, although a faint *Scd* arrival is observed in Figure 3a. At an epicentral distance of 88° the *Scd* phase arrives before the direct *S* phase as seen in Figure 3f. The amplitude of the *Scd* arrival increases with increasing epicentral distance.

From each vespagram we measured the travel time, slowness, and amplitude of the *S*, *Scd*, and *ScS* arrivals. Keeping the event depth fixed, we notice that there is a linear decrease in $\delta T_{\text{Scd-S}}$ with increasing discontinuity height above the CMB and a linear increase in $\delta T_{\text{Scd-S}}$ with increasing height (see Figures S1–S4 in the supporting information, which show the linear travel time relationships as a function of discontinuity height for four distinct distance ranges), where the measurements are made for all models in our model space. For the $\delta T_{\text{Scd-S}}$ measurements there is little discernible effect from *S* wave velocity increase beneath the discontinuity. Yet for the $\delta T_{\text{ScS-Scd}}$ measurements the *S* wave velocity increase affects the travel times that introduce scatter in the measured differential travel time as discontinuity height increases. Thus, $\delta T_{\text{Scd-S}}$ measurements, which display almost no scatter, provide a more robust height estimate. Measured differential slownesses, $\delta u_{\text{S-Scd}}$ and $\delta u_{\text{Scd-ScS}}$, are also correlated with discontinuity height. However, the range of slowness variation is small (1 s/° across the entire height range) compared to the slowness resolution attained in the vespa process. Hence, we do not use differential slowness to constrain height. Previous modeling efforts have demonstrated that to match $\delta u_{\text{S-Scd}}$ a negative velocity gradient immediately above the *D″* discontinuity is required [*Yao et al.*, 2015]. There is no correlation between measured amplitude ratios and discontinuity height. $\delta T_{\text{Scd-S}}$ shows the strongest relation to discontinuity height and hence we use these times as a basis for calculating the height of the *D″* discontinuity. To correct for event depth, we calculated the difference in *D″* discontinuity height of the

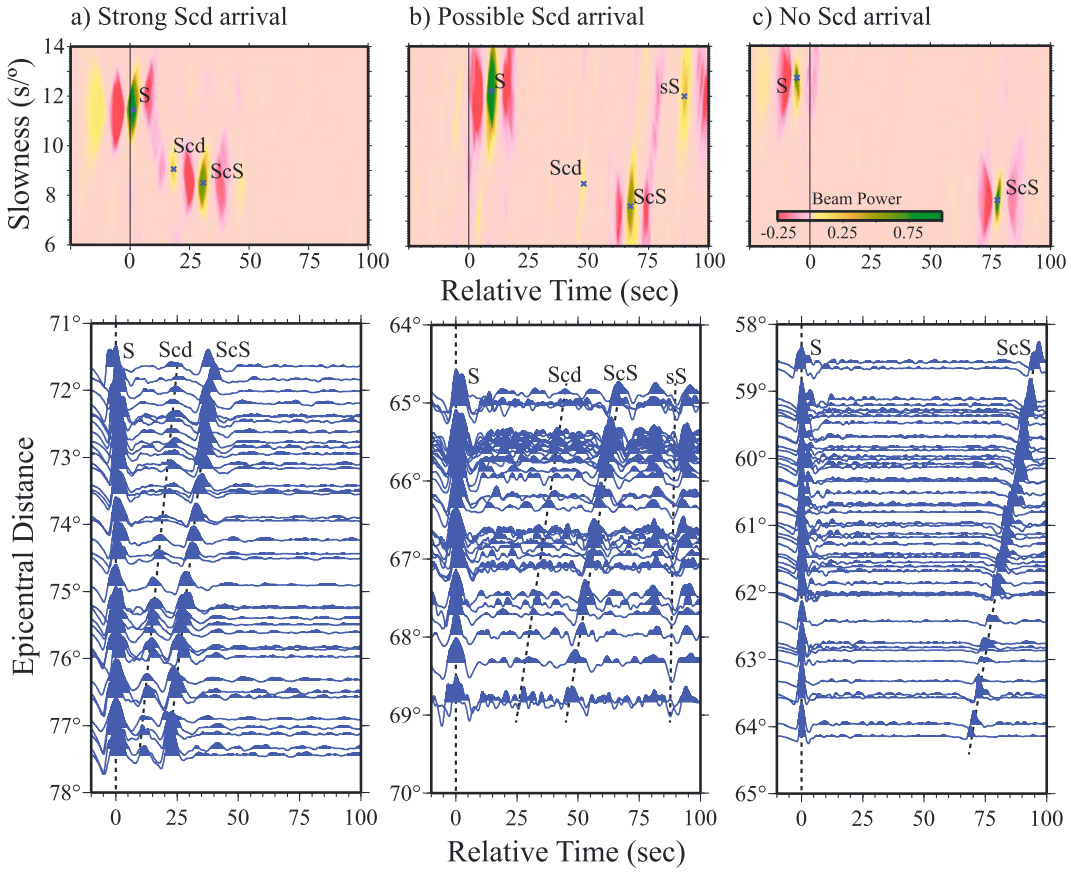

Figure 4. Vespagrams and waveforms for (a) event: 201205280507 bin M03 showing strong *Scd* arrival, (b) event: 200909050358 bin C05 showing a possible *Scd* arrival, and (c) event: 201111221848 bin L03 showing no *Scd* arrival. The displacement waveforms and vespagrams are aligned and normalized to unity on the direct *S* wave arrival.

synthetic model and the height calculated from the equations. Here we use another linear trend to account for differences in event depth.

Estimating the strength of the *S* wave velocity increase below the discontinuity is more challenging. There is no linear trend for differential travel time or differential slowness versus δV_S. Yet there is a mild correlation between $\delta A_{Scd/ScS}$ and $\delta A_{Scd/S}$ and δV_S. Of these, $\delta A_{Scd/S}$ shows the least effect from discontinuity height and also shows a nearly flat slope as a function of δV_S. This may in part be due to the *n*th root stacking process employed in computing vespagrams. There is enough scatter in $\delta A_{Scd/S}$ to make distinguishing a 1% *S* wave velocity increase from a 2% increase uncertain.

3.3. Data Analysis

We sorted our processed data (see section 2) for each event-station pair into 3° geographical bins, retaining bins that contained at least 10 stations. We treat the stations within each bin as an array for which we calculate vespagrams. We also sorted event-station pairs such that we shifted the bin centers by 1.5° in latitude and longitude, and also performed a test where we required a minimum of 20 stations per geographic bin.

We visually inspected each vespagram for *S*, *Scd*, and *ScS* phases. We only retained vespagrams that did not display a large amount of streaking in slowness that is indicative of too small of a receiver aperture. In particular, if the seismic phases exceeded a spread in slowness greater than 4 s/° we discarded the vespagram, where we defined the edge of the arrival at a beam power of 0.25 (e.g., yellow-green area in Figure 3). If the amplitude of the noise in the vespagram between the *S* and *ScS* arrivals was comparable to the amplitude of *ScS*, we discarded it. Thus, we retained only the highest-quality vespagrams with good signal-to-noise ratio and less than 4 s/° slowness resolution. We also discarded vespagrams at epicentral distances where the *Scd*

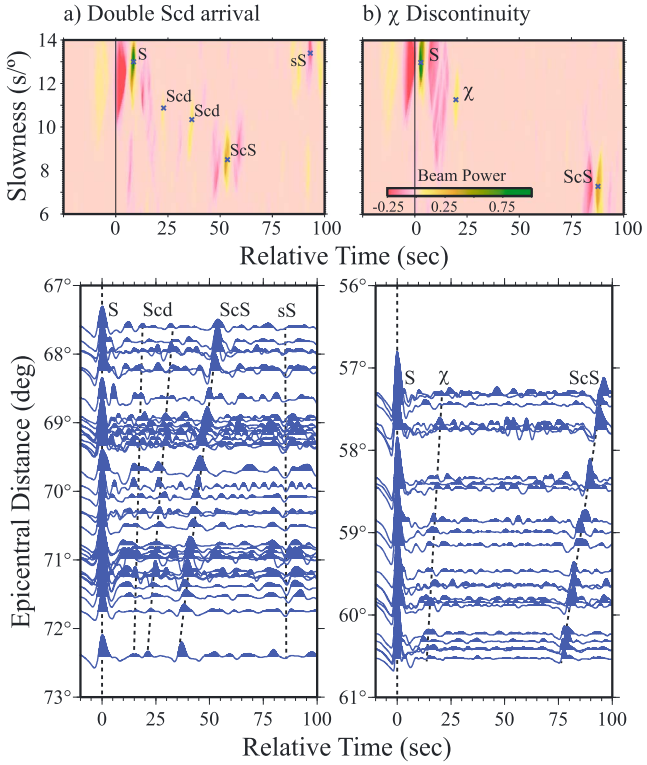

Figure 5. Vespagrams and waveforms for (a) event: 200907120612 bin E03 showing a double *Scd* arrival and (b) event: 201111221848 bin R02 shows an arrival (χ) that has an inferred height of 730 km above the CMB. The waveforms and vespagrams are aligned and normalized to unity on the direct *S* wave arrival.

arrival approached the cross-over distance with the direct *S* arrival as measuring differential travel times may be compromised by interference between the arrivals.

We classified each vespagram as follows: (1) no apparent *Scd* arrival, (2) strong *Scd* arrival, and (3) possible *Scd* arrival. We defined strong *Scd* arrivals where an *Scd* arrival was apparent, intermediate in time and slowness (must have a slowness that is $\geq$0.5 s/° from *ScS* and $\leq$0.5 s/° from *S*) between the direct *S* and *ScS* arrivals, and with amplitude exceeding the average noise level between the *S* and *sS* arrivals. The majority of all vespagrams categorized as strong *Scd* arrivals also showed clear *Scd* arrivals in record sections. Possible *Scd* arrivals are defined as arrivals intermediate in time and slowness between the *S* and *ScS* arrivals but having amplitude that is approximately equal to the average noise level as determined by visual inspection. Typically, possible *Scd* arrivals are defined as being evident in the vespagram but not clearly identifiable in record sections. In the same manner as applied to the synthetic seismograms, for each data vespagram we measured the differential travel time, slowness, and amplitude for *S*, *Scd*, and *ScS*.

4. Results

Example vespagrams and record sections that characterize the majority of our data are shown in Figure 4. Figure 4a shows an example where the *Scd* arrival is clearly visible in both raw data and the vespagram and is thus classified as a *strong Scd* arrival. Figure 4b shows an example where the *Scd* arrival is just above the noise limit and is thus classified as a possible *Scd* arrival. Figure 4c shows an example where no arrival is present between *S* and *ScS* and is thus classified as a nonobservation. Note that in the last example, the epicentral distance (array center at approximately 61°) is not the optimum distance for detecting *Scd*. Thus, a nonobservation does not necessarily imply that the *D*″ discontinuity does not exist in this location; rather its existence may be below our detection ability in this case.

In addition to the standard data behavior reported above we classify two additional types of observations, which are shown in Figure 5. Figure 5a shows an example we refer to as a double *Scd* arrival. Here there appears to be two distinct *Scd* arrivals in the vespagram. The existence of a double *Scd* arrival could be due to either a second discontinuity or discontinuity topography [*Thorne et al.*, 2007]. Figure 5b shows the final type of observation that we refer to as a χ discontinuity observation. Here we have an arrival that appears similar to an *Scd* arrival except that our inferred height is greater than 600 km. Observations of these arrivals have only been found for data within the epicentral distances of $55° \leq \Delta \leq 64°$. Neither of these types of observations is related to complicated sources as source structure would cause multiple arrivals at the same slowness, which we do not observe for these data. Similarly, arrivals from upper mantle reflections or depth phases produce arrivals where the slowness is more similar to the direct *S* wave arrival, which is not observed in either of these cases.

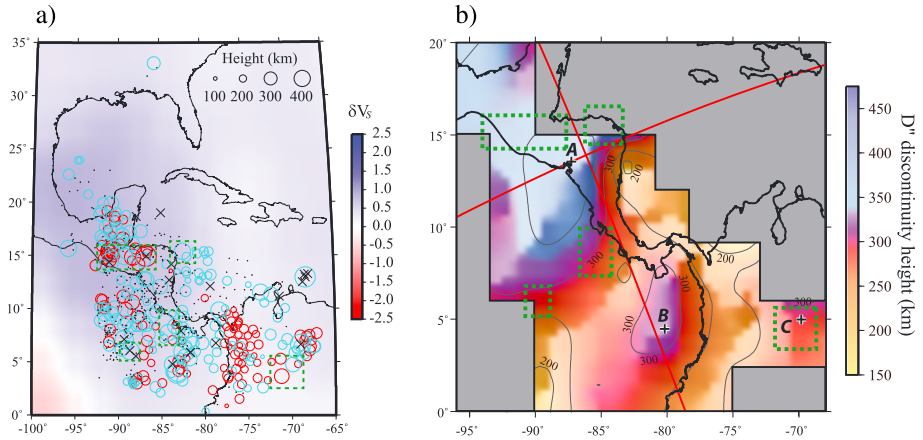

Figure 6. (a) Results for individual geographic distance bins. The red circles show the locations of *ScS* bounce points for event-array pairs that show strong *Scd* arrivals. The blue circles show possible *Scd* arrivals and the black dots show nonobservations. The large black crosses are arrivals for a possible χ discontinuity 600 to 1000 km above the CMB. The background is *S* wave velocity from model TXBW directly above the CMB [*Grand*, 2002]. The dashed green boxes highlight where double *Scd* arrivals are observed. (b) Contour map of the average height of the *D*″ discontinuity. The grey shaded areas outline where there is no data. The red lines shown are where we show cross-sectional images in Figure 8.

Figure 6a shows the raw data results. The result for each event-subarray pair is plotted at the corresponding *ScS* bounce point on the CMB. The red circles correspond to strong *Scd* arrivals and the blue circles correspond to possible *Scd* arrivals. Circle size is scaled by the height of the *D*″ discontinuity. The small black dots are nonobservations. We have a total of 125 strong *Scd* observations, 180 possible *Scd* observations, and 343 nonobservations. Observations of double *Scd* arrivals are only apparent in a limited geographic range as outlined by dashed green boxes in Figure 6 (also indicated by multiple scaled circles at the same location). There are a total of 16 double *Scd* observations and one possible triple *Scd* arrival. Additionally, there are a total of 21 χ discontinuity observations that are indicated by black crosses in Figure 6a.

In order to emphasize the overall trends in these data, we show a weighted average of *D*″ discontinuity height in Figure 6b. The weighted average is calculated with high-quality observations (strong *Scd*) given a weight of 1.0 and the medium quality observations (possible *Scd*) a weight of 0.5. We sorted data into 3° geographic bins based on the *ScS* bounce point on the CMB. We do not include the nonobservations in our weighted average calculation. With the double *Scd* arrivals we used discontinuity measurements with the greatest height in calculating our weighted average. The majority of our study region shows discontinuity heights in the range from approximately 150 to 200 km. Yet there exists a large step-up in topography (a peak in the *D*″ discontinuity peak labeled A in Figure 6b) centered at roughly 10°N and 90°W which has a maximum height of roughly 380 km above the CMB with an average height of 375 km. The locations where we observe nearly all double *Scd* arrivals (green dashed lines) clusters at the edges of peak A. We also observe two smaller peaks in the south (approximately 4°N and 83°W, peak B) and southeast (approximately 4°N and 70°W, peak C) of our study region with maximum heights of roughly 320 and 330 km, respectively. Double *Scd* arrivals are associated with peak C, but none are observed in conjunction with peak B. There is no apparent correlation between χ discontinuity observations and inferred discontinuity height.

As additional checks we produced maps where we (1) only used the strong *Scd* arrivals (Figure S5 in the supporting information), (2) used the minimum discontinuity height for double *Scd* arrivals (Figure S6), (3) shifted the bin centers for event-subarray pairs by 1.5° to the east and 1.5° to the south (Figure S7), and (4) required a minimum of 20 stations per subarray (Figure S8). The overall pattern between strong *Scd* arrival only and the weighted average of strong and possible *Scd* arrivals remains consistent. As the location of the double *Scd* arrivals occurs at the edges of inferred steep topography, using the lower height value also does not change the map appreciably. Furthermore, we find consistent results when shifting the centers of the subarray locations. In order to plot our final map (Figure 6b), we used both the original bin center locations and the shifted locations.

5. Discussion

5.1. Discontinuity Topography

Our results indicate that there is significant localized topography on the *D*″ discontinuity beneath our study region. The region of the discontinuity with the greatest height above the CMB (peak A, Figure 6b) lies beneath Honduras and Nicaragua (approximately at 10°N and 90°W) and is characterized by a step in topography of roughly 175 km over a lateral distance of roughly 200 km. A corresponding step down in topography is suggested to the northwest (approximately beneath Guatemala). Additionally, we see two smaller peaks in the south (peak B) and southeast (peak C) areas of our study region which are characterized by approximately 70–80 km of relief in 300 km. Our final height map (Figure 6b) is drawn using the greatest height measurements where double *Scd* arrivals are detected; yet using the discontinuity measurements with the smallest height also provides a solution with the same level of topography (Figure S6).

The *D*″ discontinuity in this region has been scrutinized by many previous studies. We find general agreement with the results of prior studies in regard to discontinuity height. In what follows, we summarize some of the previous results with respect to our own and discuss some of the other observations made in these studies. To assist in the interpretation, Figure S9 outlines the previous study regions overlain on our height map.

Kendall and Nangini [1996] probed a portion of our study region using *Scd* arrivals. At a location of approximately 10°N and 60°–85°W they found an average *D*″ discontinuity height of 250 km. This is in excellent agreement with our results for this region. Their study does not sample the large topographic high (Peak A) imaged in the present study, but samples north of this peak at approximately 20°N and 80°–90°W, finding that the discontinuity height increases to 290 km. This agrees with the increased discontinuity height to the North inferred in our study, although we do not sample this region as thoroughly as *Kendall and Nangini* [1996]. *Kendall and Shearer* [1994] also examined a small region beneath Columbia finding an average discontinuity thickness of 280 km. This could correspond to the slight rise in topography (up to 300 km) we image.

In *Lay et al*. [2004] the discontinuity is modeled in four discrete geographical bins (Bins 1–4 in Figure S9a) using a double-array stacking method. They observe a general trend of discontinuity height increasing to the north, with weak or nonexistent *Scd* arrivals in Bin 2. Our minimum discontinuity height is found in Bin 1 (188 km) but on average is thicker than that found by *Lay et al*. [2004] who found a 160 km discontinuity. We also find a region where many nonobservations are located roughly corresponding to the region Bin 2. However, the zone of weak or nondetections in our study extends beyond the Bin 2 region to the northeast. We are in agreement with a discontinuity height in this region of about 260 km. Bin 3 shows a height of 240 km, whereas we find the discontinuity starting to increase in height more rapidly in this region (~300 km). Two arrivals are inferred at Bin 4 from the study of *Lay et al*. [2004], one at 210 km and another at 380 km. The second arrival at 380 km fits well with our maximum height of 375 km for this region. But we note that we also observe multiple arrivals in this region and that we interpret the maximum height arrival as due to the *D*″ discontinuity. Alternatively, *Lay et al*. [2004] model the region with a flat discontinuity of 264 km with *S* wave velocity variation in each bin. This is not far from our average height of 297 km, nevertheless, *Thorne et al*. [2007] discussed the challenges associated with concatenating small geographic bins together to form a composite model and showed that tomography model TXBW [*Grand*, 2002] with an artificial discontinuity 220 km above the CMB and varying *S* wave velocity beneath provided a better fit to those data. The effect of *D*″ velocity heterogeneity is discussed below and in Figures S11–S14.

Kirchoff migration methods have been used to image the discontinuity in two separate studies. First, *Thomas et al*. [2004] found a lateral step-up in discontinuity topography that roughly corresponds in shape to that found in our study. They find a discontinuity height of roughly 150 to 300 km increasing in height rapidly to the North. We generally find a greater discontinuity height, but the pattern of observed topography is the same. Second, *Hutko et al*. [2006] also observed the step in topography ranging from about 175 km to 300 km. Their study does not cross the maximum topographic high imaged in this study, but their height and location of the step are in good agreement with the present study. *Shang et al*. [2014] used a Radon Transform technique to stack *ScS* arrivals. They found a relatively flat discontinuity ranging between 250 and 300 km in height. The overall shape of discontinuity topography uncovered by *Shang et al*. [2014] appears similar to the present study, however, muted in amplitude.

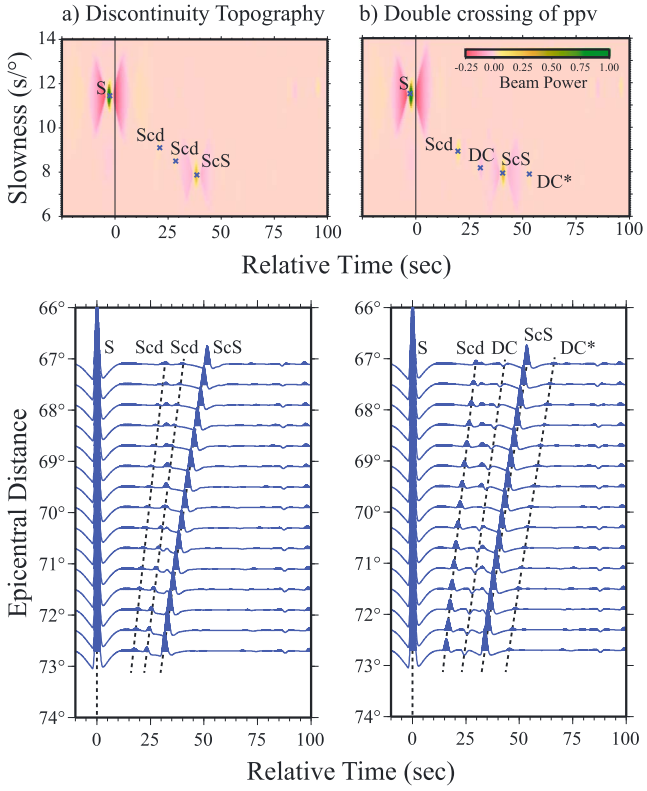

Figure 7. (a) Vespagrams and waveforms for topographic model which has a *D*″ discontinuity starting height of 150 km with a 150 km step and a δV_S of 2%. Two *Scd* arrivals are observed. (b) Vespagrams and waveforms for a double-crossing model with a discontinuity at 300 km above the CMB with a δV_S of 2% and a second discontinuity 50 km above the CMB with a δV_S of 0% with respect to the PREM model. *S* wave velocity model is shown in Figure S20 in the supporting information. The waveforms and vespagrams are aligned and normalized to unity on the direct *S* wave arrival. Two additional arrivals are observed: (1) DC: a reflection off of the top of the low-velocity contrast (in TauP toolkit [*Crotwell et al*., 1999] notation the phase is named *Sv2841S*), and (2) DC*: an underside reflection off the low-velocity contrast (in TauP notation this arrival is named *ScS^2841ScS*). We note that 2841 km is the radius of the low-velocity contrast in this model.

In order to assess the effect of topography, *Thorne et al*. [2007] examined synthetic seismograms for a step in discontinuity topography finding that two *Scd* arrivals should exist. We calculated synthetics for a series of models with a step in topography. Figure 7 displays the vespagrams and waveforms for one of these models with a 150 km step-up in topography. Figure 7a shows that two *Scd* arrivals are observed in the vespagram and synthetic waveforms. Analysis of synthetic seismograms with different step locations shows that the double *Scd* arrival only occurs when the *Scd* turning point is near the step location, within approximately 5° of the edge of the step and is observed regardless of whether the step is up or down (see Figure S10). Figure 6b shows the locations where we observe double *Scd* arrivals as gray dashed boxes. Note that near our largest inferred step in topography we see double *Scd* arrivals ringing its edges, yet no double *Scd* arrivals are observed within. Thus, we interpret the presence of two *Scd* arrivals as due to a step in topography, where our observations of the two reflectors coincide with the strongest gradients in topography. If two reflectors were laterally continuous we would expect to see them in the center of the topographic high as well. Further synthetic testing should be carried out in future studies to examine how sharp the step in discontinuity topography must be in order to generate double *Scd* arrivals.

Our inferred discontinuity structure also includes a step in topography in the lateral, off great-circle path, direction. As noted in *Sun and Helmberger* [2008] additional waveform distortions may occur for paths sampling near these lateral steps in topography. Most notably, a double *Scd* arrival may also occur along these boundaries, which we may observe along the eastern boundary of the step (see Figure 6). It is also possible that some of the double *Scd* arrivals we observed were generated by off great-circle path structure. We computed vespagrams for double *Scd* arrival event-array pairs where we allowed the back azimuth to vary. For these observations the energy stacked at a maximum along the great-circle path indicating significant energy is not arriving from out-of-plane directions. Nevertheless, we did not systematically search all event-array pairs for significant off great-circle path arrivals. Future efforts should look for such arrivals as indicative of strong 3-D structural effects.

The region beneath the large topographic high in our study is underlain by the highest *S* wave velocities imaged in tomographic models (Figure 6a). Figure 8 shows cross sections through tomography model TXBW [*Grand*, 2002] for our study region and shows that the seismic velocity is at its highest beneath the large step we observe. *Thorne et al*. [2007] examined synthetic seismograms computed with this tomography

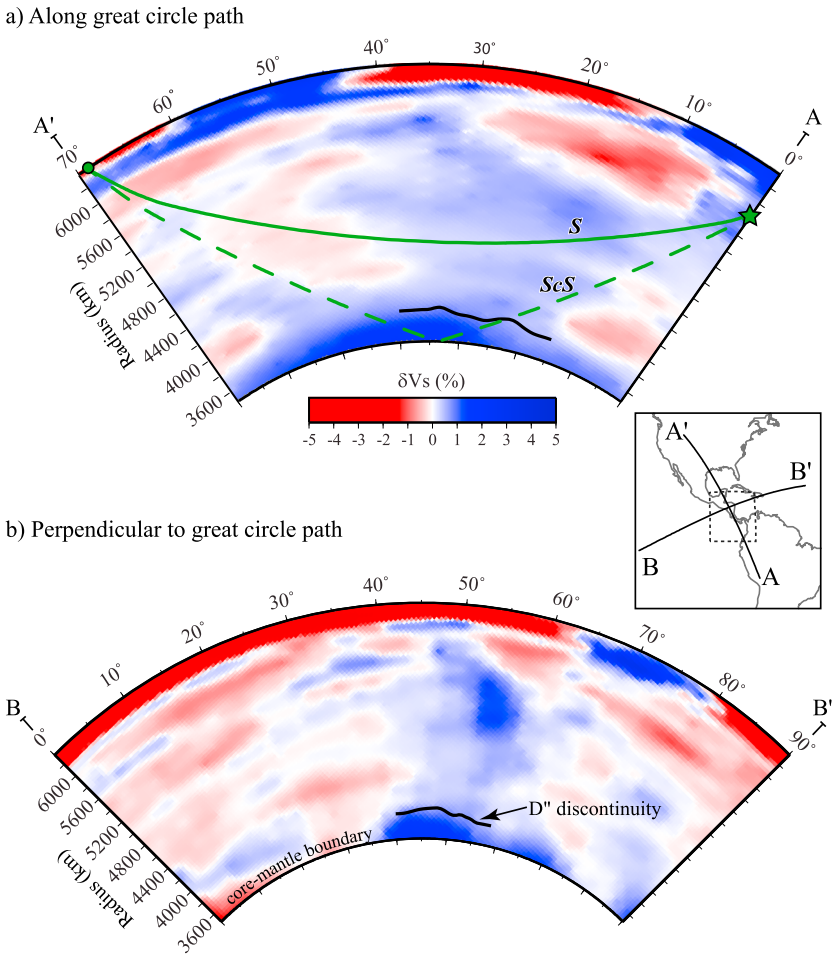

Figure 8. Cross sections through *S* wave tomography model TXBW. (a) Cross section is shown through great-circle path from an event location at 15.0°S and 70.4°W and a receiver location at 43.8°N and 109.2°W. Ray paths are drawn for direct *S* (solid green line) and *ScS* (dashed green line) for a 500 km deep event at an epicentral distance of 69°. The solid black line shows inferred *D″* discontinuity along this cross section. (b) Cross section perpendicular to that shown in Figure 8a.

model for paths crossing through our study region and concluded that model TXBW provided a best fit to *D″* discontinuity observations. However, in that study the portion of the discontinuity with the maximum height (in Bin 4 of *Lay et al*. [2004]) was not fit by model TXBW alone. The relationship between *S* wave velocity and discontinuity was also examined in *Sun et al*. [2006]. They demonstrated that the increase in seismic velocity and discontinuity topography trades off with each other but that seismic velocity increase beneath the topographic high is not enough to account for *Scd-S* differential travel times alone and that some amount of topography is necessary. Nonetheless, the trade-off between velocity and height implies that our discontinuity height in this region may be somewhat elevated as the upgoing *Scd* paths will be sped up in the presence of the topographic high. Midmantle seismic heterogeneity can also affect the *Scd-S* differential times used in estimating discontinuity height [e.g., *Yao et al*., 2015]. In our study region there are significant regions of midmantle high wave speeds due to the subducting Farallon slab. These high wave speeds may have the effect of increasing the *Scd-S* differential times and making the discontinuity appear deeper. As prescribed in *Thorne et al*. [2013], we assess these effects by computing synthetics through cross sections of tomography and also hybrid models, where we modify tomography models by our discontinuity height estimates.

We computed synthetic seismograms through cross sections of *S* wave velocity model TXBW [*Grand*, 2002] for four great-circle paths. We chose paths that have central *ScS* bounce points at locations of (1) 5°N, 75°W, (2) 10°N, 80°W, (3) 10°N, 85°W, and (4) 10°N, 90°W, for events on (1) 28 May 2012, (2) 21 July 2007, (3) 1 January 2011, and (4) 24 March 2008, respectively (see Table S1 for event details). Synthetic seismograms

and synthetic vespagrams are compared side by side with data for these paths in Figures S11–S14. The *Scd* arrival in these models is due to an artificial discontinuity between roughly +1.5 and 2.0% in the TXBW model 220 km above the CMB [*Thorne et al*., 2007]. For each path the relative timing between the *S*, *Scd*, and *ScS* arrivals are in excellent agreement. The slowness of the arrivals is also in good agreement for all paths except for path 4 (10°N, 90°W). For path 4 the slowness of the *Scd* arrival is significantly lower (by 1 s/°) than that observed in the data. This path samples the region of the *D*″ discontinuity where we find the maximum discontinuity height. If the discontinuity height is greater than the 220 km layer thickness of the TXBW model, the *Scd* arrival should arrive at the array with a shallower incidence angle (i.e., larger slowness). Hence, these data suggest a discontinuity at a greater height above the CMB than is provided by the artificial discontinuity in model TXBW. Depending on the event, the dominant period of the direct *S* wave varies from roughly 7 to 10 s. This variability in source time characteristics may introduce some error in our measurements as our measurements are taken from the peaks in the vespagrams. Most notably $\delta T_{\text{Scd-S}}$ may be affected as the direct *S* wave has been noted in previous studies [*Ford et al*., 2012] to be more attenuated than lower mantle phases such as *ScS*. This increased attenuation of the *S* wave would effectively reduce the $\delta T_{\text{Scd-S}}$ times as our measurements are made between peaks in the vespagrams. However, synthetic tests through model TXBW computed for source time function dominant periods between 5 and 15 s show identical results. Nevertheless, tomography models may underestimate the strength of the velocity anomaly in the downgoing slab [*Ford et al*., 2012] which gives rise to the possibility of a bias of shorter *Scd-S* measurement in our study which may also artificially increase our discontinuity height estimate.

We next overlaid our *D*″ discontinuity model onto the four cross sections of tomography outlined above. We construct these hybrid models by first setting our *S* wave velocities as given by the cross sections of tomography. Then we impose our inferred *D*″ discontinuity topography (model shown in Figure 6b) with a 2% *S* wave velocity jump for the four different paths (synthetic seismograms for our topography model not embedded in *S* wave tomography are shown in Figures S15–S18). Beneath the discontinuity we set a linear gradient in δV_S from a radius of 3600 km down to the CMB to preserve *ScS* travel times. At the CMB the *S* wave velocity is set at −4% relative to the tomography model values. Results for the four paths are shown in Figure 9. Inclusion of our discontinuity structure has the following effects. First, the amplitude of the *Scd* arrival is generally higher than for synthetics computed in TXBW alone. This indicates that some degree of *S* wave velocity increase greater than what is provided by TXBW is necessary. Second, the *Scd-S* differential travel times are similar to what is observed in these data suggesting that we are not strongly influenced by midmantle seismic heterogeneity. Finally, the tomography model does an excellent job of recovering *ScS-S* differential travel times. In order to unravel the seismic velocity structure of the deep mantle in the Central American region, future tomography efforts will need to include *Scd* arrivals in their inversions.

5.2. Low *S* Wave Velocity Reflectors

Several studies have discussed observations of reflectors in this region with a negative impedance contrast [*Kawai et al*., 2007; *Kito et al*., 2007; *Shang et al*., 2014; *Thomas et al*., 2004; *van der Hilst et al*., 2007]. It is possible to have a negative polarity arrival as a result of a phase transition from postperovskite back to bridgmanite [*Hernlund et al*., 2005]. However, as discussed in *Flores and Lay* [2005] it is challenging to observe this secondary arrival. Figure 7b shows vespagrams and synthetic seismograms calculated for a model that has a double crossing of the postperovskite boundary. If the double crossing exists, it is expected to produce a second, negative polarity arrival, intermediate in time and slowness between *Scd* and *ScS*. We examined the vespagrams for all good *Scd* observations for this secondary arrival and were unable to identify any vespagrams that demonstrated this structure in our study region. Both *Thomas et al*. [2004] and *Kito et al*. [2007] show a negative reflector between longitudes 88°–93°W and latitudes 5°–12°N. Yet our vespagrams for *ScS* bounce points in this region do not show any clear arrivals in between *Scd* and *ScS*. The narrow band filter we used to process our data might mask where the double crossing exists, as it is expected the transformation back to postperovskite would occur at a shallow height above the CMB. In this case, the negative polarity arrival we searched for would be overprinted by the negative polarity downswing preceding the *ScS* arrival.

In addition to the negative polarity arrival mentioned in the previous paragraph, the synthetic seismograms for the double-crossing models show an additional positive polarity *ScS* postcursor (Figure 7b). This postcursor is a reflection from the underside of the low-velocity contrast for the upgoing *ScS* arrival. We also searched our vespagrams for this arrival but found no evidence of its existence in the data set. Figure 4a shows what

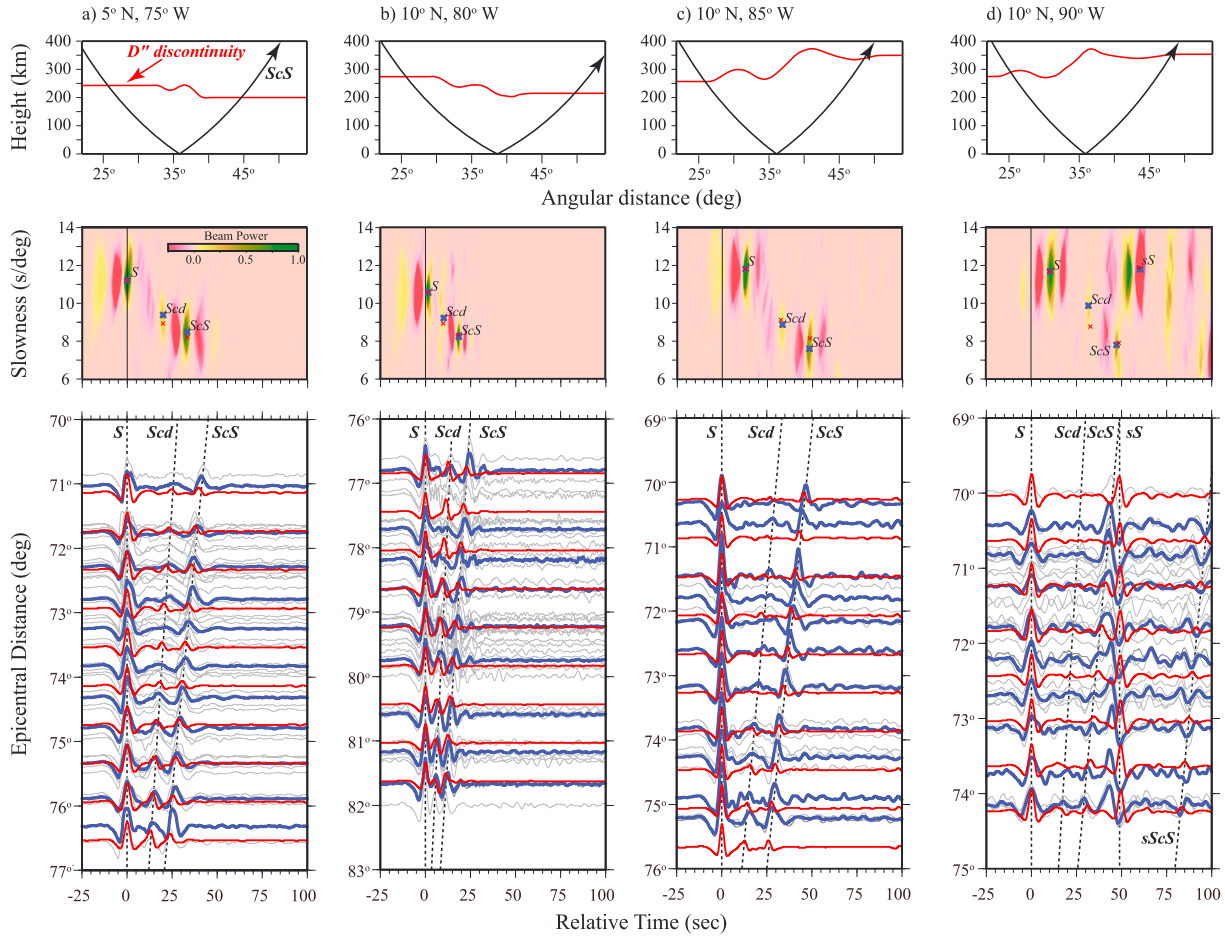

Figure 9. Vespagrams and seismograms for different paths through our study region. (top row) The *D*″ discontinuity structure (red line) from our model as height above the CMB. For reference, the *ScS* ray path between event and array center is drawn with the black line. (middle row) The vespagram for data. The blue crosses indicate the peak of the arrival in slowness and time. The red crosses indicate the peak of the arrival for vespagrams calculated based on synthetic models. (bottom row) Raw seismic traces (gray lines), stacks of data in 0.5° epicentral distance bins (blue lines), and synthetic seismograms (red lines). All seismic traces are transverse component displacement seismograms aligned on the direct *S* wave arrival. Examples are shown for paths with *ScS* CMB bounce points at (a) 5°N, 75°W, (b) 10°N, 80°W, (c) 10°N, 85°W, and (d) 10°N, 90°W.

may at first glance appear to be this *ScS* postcursor. However, that particular event exhibits source complexity that manifests as secondary arrivals at the same slowness as the main arrivals. Such source complexity can make observation of this postcursor challenging.

There are two areas where our vespagrams indicate a possible low-velocity contrast above the *D*″ discontinuity. One vespagram with an *ScS* bounce point centered at 91.3°W and 19.2°N shows a negative polarity arrival intermediate in both time and slowness between *S* and *Scd* (Figure S19a). However, none of the vespagrams with *ScS* bounce points in the surrounding area also show this arrival. In addition, a negative polarity arrival is observed for an *ScS* bounce point at 82.9°W and 4.3°N (Figure S19b). A search of vespagrams for neighboring bounce points also does not show any clear negative polarity arrivals. These areas are interesting as a low *S* wave velocity contrast may exist in these regions. However, we require multiple events to show evidence for negative polarity arrivals to have confidence that a low-velocity contrast indeed exists.

5.3. Nonobservations

In this study we had 343 vespagrams with nonobservations of the *Scd* arrival. We emphasize that a nonobservation does not necessarily imply that the *D*″ discontinuity is not present in the region. One possibility is that the discontinuity is not sharp in this region. If the discontinuity occurs gradually over a velocity transition zone, the *Scd*/*S* amplitude ratio decreases [e.g., *Yao et al.*, 2015], making detection of the discontinuity

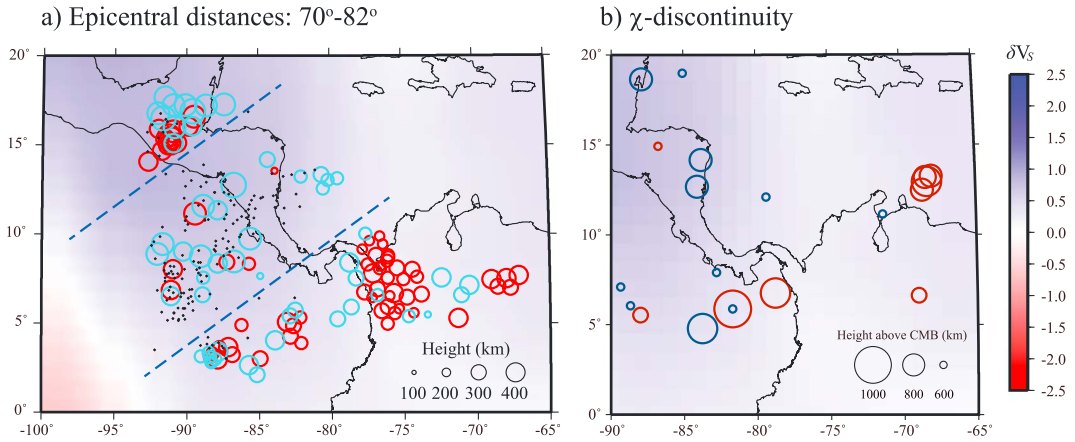

Figure 10. (a) Results for data recorded within the epicentral distance range: $70° \leq \Delta \leq 82°$. The red circles show the locations of *ScS* bounce points for event-array pairs that show strong *Scd* arrivals. The blue circles show possible *Scd* arrivals and the black dots show nonobservations. The dashed blue line separates three possible distinct regions of waveform behavior. (b) χ discontinuity observations (red circles are highest-quality observations and blue circles are medium quality observations) are plotted as a function of height above the CMB. The background is *S* wave velocity model TXBW directly above the CMB [*Grand*, 2002].

more challenging. Another possibility is that the source-receiver geometry is not optimal for detecting the discontinuity; specifically, the *Scd*/*S* amplitude ratio decreases as a function of decreasing epicentral distance. At shorter epicentral distances, the *Scd* arrivals amplitudes may simply fall below the signal detection limit of our methodology. In order to assess whether the nonobservations are related to nonoptimal source-receiver distances, we plot the locations of our observations (*strong*, *possible*, and *non*observations) for epicentral distances between 70° and 82° in Figure 10. This distance range gives us the best possible chance for detecting the *D*″ discontinuity if it exists. What we observe is that our data can be separated into three distinct regions. (1) In the northernmost region (~90°W, 15°N) the majority of the observations indicate strong or possible discontinuity observations. (2) In the southernmost region we have another band of mostly strong or possible *Scd* observations, with a major collection of strong *Scd* observations on the eastern edge (~76°W, 7°N). (3) There is a central band, approximately 8.5° wide (roughly 500 km wide on the CMB) where the nonobservations are clustered. We also plot the average epicentral distance of our observations as a function of *ScS* bounce point location in Figure S21. If we only consider nonobservations of the *Scd* arrival, we note that the central band of nonobservations consists of data primarily recorded in the distance range from 70° to 85°, and thus we do not see a bias of shorter epicentral distance event-array pairs causing the large cluster of nonobservations.

The distinctive band of nonobservations overlaps an area previously observed to lack strong *Scd* arrivals [*Lay et al.*, 2004; *Thomas et al.*, 2004]. One possible explanation for this lack of clear *Scd* arrivals is that the large topographic step in the discontinuity backscatters much of the *Scd* energy [*Thomas et al.*, 2004]. However, *Thorne et al.* [2007] showed that topography tends to produce multiple *Scd* arrivals and does not significantly scatter *Scd* energy. Another possibility is that no *D*″ discontinuity actually exists in this region. To test our observations against these various scenarios, we computed synthetic seismograms for a series of models with a hole (and without a hole) in the *D*″ discontinuity. Synthetics are computed for a 500 km deep source and a base *D*″ discontinuity model with a 300 km height and a 2% *S* wave velocity increase. We computed synthetics where we allowed the length of the hole in the great-circle arc direction to be 2°, 4°, 6°, 8°, or 10°. And we allowed the center position of the hole to be at an angular distance from the source at 32°, 34°, 36°, or 38° (a total of 20 synthetic models).

Results for the synthetic tests with a *D*″ discontinuity hole are shown in Figure S22. We emphasize the following waveform effects from these tests: (1) as the length of the hole is increased, the *Scd*/*S* amplitude ratio decreases; (2) for hole lengths up to 6° there is still an observable *Scd* arrival, even though the wave field is interacting with a gap in the discontinuity; (3) for hole lengths $\geq$6° at some distances the *Scd* arrival is no longer visible, and in general the *Scd*/*S* amplitude ratio is dramatically reduced. These results suggest that the *D*″ discontinuity may not be laterally continuous in our study region. For example, if the hole has an 8°

length (as possibly suggested by our data, see Figure 10a), and we are attempting to observe *Scd* at an epicentral distance of 76°, the amplitude should be reduced by a factor of 3. Nonetheless, we note that the grazing geometry of the *Scd* wavefield does not always rule out the observance of an *Scd* arrival, rather that if a hole exists it could significantly affect the *Scd* amplitudes depending on the source-receiver geometry, making the *Scd* arrival sometimes visible and sometimes not visible.

The synthetics described above have a *D*″ discontinuity that is equal in height on either side of the hole. If the hole is not equal in height on either side of the discontinuity, multiple *Scd* arrivals are generated. For example, we computed synthetics where the discontinuity height was 200 km on the receiverside of a 4°-wide hole centered on an *ScS* bounce point of 36° (compare with Figure S22b) and 400 km on the sourceside of the hole. Multiple *Scd* arrivals are apparent for epicentral distances from 64° to 73°. Multiple *Scd* arrivals are similar to models with a step in topography as discussed previously; however, the arrivals are generated for a larger range of epicentral distances. Nonetheless, a hole with varying height discontinuity on either side of the hole is another possible explanation for our observations of multiple *Scd* arrivals at approximately 90°W 5°N and 85°W 8°N.

Anisotropy measurements for the region may provide additional insight. Both composition and mantle flow direction can significantly affect the fast direction of seismic wave speeds as well as the amplitude of *Scd* arrivals [e.g., *Thomas et al*., 2011]. *Rokosky et al*. [2004] performed a detailed study of anisotropy in a subset of our study region also using South America earthquakes recorded in North America with similar wave paths to our study. Their results may also be discussed in terms of the three geographic bands we show in Figure 10a (see also Figure S23). In the southernmost band *Rokosky et al*. [2004] show mostly *SH*-fast wave speeds. In this southern region they also observe *Scd* splitting with *Scd* on the transverse component being fast. The central band shows a large mix of anisotropy measurements with both *SH* and *SV* fast but relatively weak anisotropy. The northern band is mostly *SH* fast with the largest anisotropy measurements being in this location.

For most slab subduction geometries, slip on (001) planes in postperovskite will generate *SH*-fast shear wave splitting [*Cottaar et al*., 2014; *Miyagi et al*., 2010; *Wenk et al*., 2011]. On the other hand, if the slab is dominantly bridgmanite rather than postperovskite, *SV* should be fast [*Cottaar et al*., 2014; *Wenk et al*., 2011]. One possibility is that the northern and southern bands are composed of postperovskite, while the central band is composed of bridgmanite. In this scenario, the *D*″ discontinuity is the result of the bridgmanite to postperovskite phase transition, which is apparent in the northern and southern bands. The (a) mixed anisotropy and (b) weak *D*″ discontinuity observations in the central region are explained by *ScS* and *Scd* paths sampling a mixture of both bridgmanite (*SV* fast and no *D*″ discontinuity) in the central band and postperovskite (*SH* fast and prominent *D*″ discontinuity) in the northern and southern bands. Since enrichment of mid-ocean ridge basalt (MORB) leads to the postperovskite transition occurring higher above the CMB [*Grocholski et al*., 2012; *Ohta et al*., 2008], the greater height discontinuity observed in the northern and southern bands would be consistent with localized presence of slab material. As diffusion rates are on the orders of meters per billions of years [e.g., *Ammann et al*., 2010; *Yamazaki et al*., 2000], this chemical heterogeneity can be maintained over geologic time, and thus the central band would remain predominantly bridgmanite.

One possible explanation for two distinct regions of MORB enrichment is that the Farallon slab has locally dripped at the northern and southern bands but is absent in the central band. Alternately, the subduction history of the region may be more complex than a single Farallon slab subduction event. For example, *Sigloch and Mihalynuk* [2013] speculate that an older subduction event which they refer to as the Mezcalera subduction component may be separate from the southern Farallon slab components. Their interpretation of these past subduction events suggests that what we observe as *D*″ discontinuity in the southernmost band may be related to the Mezcalera subduction component and that our observations in the northernmost band may be related to Farallon slab components. If this is correct, we are observing *D*″ discontinuity structure associated with two distinct subduction events, the slabs of which have dripped nearly vertically and are not connected with one another.

In the presence of subducting slabs anisotropy measurements become generally more complicated. For example, in the vertically downwelling portion of the slab relatively weak anisotropy is produced with a mixture of *SH* and *SV* fast, whereas in the flattened out portions on the CMB *SH* is generally fast [*Cottaar et al*., 2014]. Thus, another possibility is that the central band corresponds to an area where the downwelling Farallon slab is near vertical generating mixed *SH*- and *SV*-fast observations. As the downwelling slab flattens

out to the north and south we have *SH*-fast observations. Although this could be consistent with a slab that has piled up and folded back on itself, similar to *Hutko et al*. [2006], this scenario is still difficult to reconcile with the expected geometry of subducting Farallon plate.

5.4. χ Discontinuity

We noted 21 *Scd*-like arrivals with an inferred height above the CMB from 600 to 1000 km that we have broadly termed as χ discontinuity observations (Figure 10b). These observations were only noticed in the epicentral distance range of $55° \leq \Delta \leq 64°$. As discontinuity height above the CMB increases, the epicentral distance where an *Scd*-like arrival is apparent decreases. For example, we computed synthetic seismograms for a *D*″ discontinuity 800 km above the CMB with a 500 km source depth. In this case, an *Scd* arrival is apparent at epicentral distances up to 68°, after which *Scd* merges with and then crosses over the direct *S* wave. In this study we did not collect data for epicentral distances less than 55°; thus, it is not surprising that our observations of an unknown discontinuity at heights of roughly 600–1000 km were constrained to the limited distance range reported.

It is unlikely that these 21 χ discontinuity observations can be explained by a bridgmanite to postperovskite phase transformation, as for most possible mineralogical assemblages the predicted transformation occurs at heights less than 700 km above the CMB [*Grocholski et al*., 2012]. The one possible exception is with the addition of Fe^{2+}. However, addition of Fe should lower seismic *S* wave velocities whereas our observations are underlain by some of the highest *S* wave velocities in the deepest mantle, thus making large amounts of Fe addition unlikely. No other study to our knowledge has identified reflectors in this range of heights above the CMB. *Courtier and Revenaugh* [2008] have observed reflectors using multiple *ScS* reverberations in our study area from approximately 1360 to 1500 km above the CMB, which are above the reflectors we have identified. The reflectors in *Courtier and Revenaugh* [2008] have their greatest height at the westernmost end of our study region and gradate closer to the CMB to the east. This spatial pattern does not correlate with the pattern we observe (Figure 10b), yet the observations of these reflectors and their link to subducting Farallon slab suggests that this subducted material may be responsible for the reflectors we observe as well. Additional observations of anomalous midmantle *S* wave broadening suggests that the ancient Farallon slab material is more seismically anomalous than shown in tomographic images [*Ford et al*., 2012] which also lends support toward these reflectors being related to slab material. There does not appear to be any correlation between the height of our observations and *S* wave velocity from tomography, inferred *D*″ discontinuity height, or strong *Scd* arrivals.

We used a modified version of our vespagram processing technique to stack in both slowness and back azimuth to determine if these χ discontinuity arrivals were coming in along the great-circle arc direction. We examined the nine highest-quality χ discontinuity observations and observed that the energy associated with these arrivals is arriving along the great-circle arc direction. Thus, these arrivals may be associated with flat-lying discontinuity structure. Further work should consider even shorter epicentral distance ranges than considered in this study to determine the full extent of such arrivals in this region. We also searched through our data for traces near epicentral distances of 70°, which is near the predicted cross-over location between direct *S* and the χ discontinuity arrivals. However, we were unable to directly confirm the existence of χ discontinuity arrivals in individual seismic traces. Future studies should also consider looking for these arrivals.

6. Conclusions

The average *D*″ discontinuity height in our study area is 286 ± 6 km with a minimum height of 188 and a maximum height of 380 km. Multiple studies examining the deepest mantle beneath Central America are now converging on a picture where the *D*″ discontinuity has large topographic relief. The largest topographic feature in our study has an average height of 375 km; however, we see a maximum height that locally rises to nearly 400 km. Localized enrichment of MORB can increase the height of the *D*″ discontinuity to 400 km [*Grocholski et al*., 2012; *Ohta et al*., 2008], and thus, the localized increase in discontinuity height reported here could be related to past subduction of the Farallon slab. Linking past subduction to current features on the core-mantle boundary is somewhat speculative, and models of subduction history [e.g., *Lithgow-Bertelloni and Richards*, 1998] show that subduction of the Farallon plate likely occurred farther to the east of the present location of subduction in Central America. Yet viscosity increases in the deepest mantle could cause slab structure to broaden and circum-Pacific high-velocity anomalies may indeed be the final resting place of slabs [e.g., *Grand et al*., 1997]. A high-velocity feature in model TXBW is present connecting the surface to the CMB

(see Figure 8) and could be related to Farallon slab material. If the slab gets folded over on itself (as suggested in *Hutko et al*. [2006]), then localized regions of high MORB concentration could explain laterally heterogeneous discontinuity height as well as possible reflectors at shallower depths (our χ discontinuity observations). Localized drips of slab material or distinct subduction events could produce regions where the discontinuity is apparent through the bridgmanite to postperovskite transition but absent in nearby regions where the slab material has not affected the lower mantle. The expanding wealth of data generated through projects such as Earthscope has allowed us to employ well-known array processing methods and revealed previously unseen detail in deep mantle structure. There are a large number of potential arrivals revealed within this data set for which the origin is currently unknown or only guessed at. Future efforts should take advantage of these processing techniques applied to three-component broadband data to further refine our knowledge of deep Earth structure and processes.

Acknowledgments

We gratefully acknowledge the University of Utah Center for High Performance Computing (CHPC) for computer resources and support. M.T. and S.W. were partially supported by NSF grant EAR-1014749. N.S. was partially supported by EAR-1361325 and EAR-1447041. L.M. was partially supported by NSF grant EAR-1344579. Figures were drawn using the Generic Mapping Tools [*Wessel and Smith*, 1998]. We acknowledge two anonymous reviewers whose comments improved this manuscript. Data used in this study may be downloaded from http://web.utah.edu/thorne/data.html.

References

Ammann, M. W., J. P. Brodholt, J. Wookey, and D. P. Dobson (2010), First-principles constraints on diffusion in lower-mantle minerals and a weak D″ layer, *Nature*, *465*, 462–465, doi:10.1038/nature09052.

Avants, M., T. Lay, S. A. Russell, and E. J. Garnero (2006), Shear velocity variation within the D″ region beneath the central Pacific, *J. Geophys. Res.*, *111*, B05305, doi:10.1029/2004JB003270.

Chaloner, J. W., C. Thomas, and A. Rietbrock (2009), *P*- and *S*-wave reflectors in D″ beneath southeast Asia, *Geophys. J. Int.*, *179*, 1080–1092, doi:10.1111/j.1365-246X.2009.04328.x.

Cobden, L., and C. Thomas (2013), The origin of D″ reflections: A systematic study of seismic array data sets, *Geophys. J. Int.*, *194*(2), 1091–1118, doi:10.1093/gji/ggt152.

Cottaar, S., M. Li, A. K. McNamara, B. Romanowicz, and H.-R. Wenk (2014), Synthetic seismic anisotropy models within a slab impinging on the core-mantle boundary, *Geophys. J. Int.*, *199*, 164–177, doi:10.1093/gji/ggu244.

Courtier, A. M., and J. Revenaugh (2008), Slabs and shear wave reflectors in the midmantle, *J. Geophys. Res.*, *113*, B08312, doi:10.1029/2007JB005261.

Crotwell, H. P., T. J. Owens, and J. Ritsema (1999), The TauP toolkit: Flexible seismic travel-time and ray-path utilities, *Seismol. Res. Lett.*, *70*, 154–160.

Dziewonski, A. M., and D. L. Anderson (1981), Preliminary reference Earth model, *Phys. Earth Planet. Inter.*, *25*, 297–356.

Flores, C., and T. Lay (2005), The trouble with seeing double, *Geophys. Res. Lett.*, *32*, L24305, doi:10.1029/2005GL024366.

Ford, S. R., E. J. Garnero, and M. S. Thorne (2012), Differential *t** measurements via instantaneous frequency matching: Observations of lower mantle shear attenuation heterogeneity beneath western Central America, *Geophys. J. Int.*, *189*, 513–523, doi:10.1111/j.1365-246X.2011.05348.x.

Gaherty, J. B., and T. Lay (1992), Investigation of laterally heterogeneous shear velocity structure in D″ beneath Eurasia, *J. Geophys. Res.*, *97*(B1), 417–435, doi:10.1029/91JB02347.

Garnero, E. J., D. V. Helmberger, and S. P. Grand (1993), Preliminary evidence for a lower mantle shear wave velocity discontinuity beneath the central Pacific, *Phys. Earth Planet. Inter.*, *79*, 335–347.

Grand, S. P. (2002), Mantle shear-wave tomography and the fate of subducted slabs, *Philos. Trans. R. Soc., A*, *360*, 2475–2491, doi:10.1098/rsta.2002.1077.

Grand, S. P., R. D. van der Hilst, and S. Widiyantoro (1997), Global seismic tomography: A snapshot of convection in the Earth, *GSA Today*, *7*(4), 1–7.

Grocholski, B., K. Catalli, S.-H. Shim, and V. B. Prakapenka (2012), Mineralogical effects on the detectability of the postperovskite boundary, *Proc. Natl. Acad. Sci. U.S.A.*, *109*(7), 2275–2279, doi:10.1073/pnas.1109204109.

He, Y., and L. Wen (2012), Geographic boundary of the "Pacific Anomaly" and its geometry and transitional structure in the north, *J. Geophys. Res.*, *117*, B09308, doi:10.1029/2012JB009436.

Hernlund, J. W., C. Thomas, and P. J. Tackley (2005), A doubling of the post-perovskite phase boundary and structure of the Earth's lowermost mantle, *Nature*, *434*, 882–886, doi:10.1038/nature03472.

Houard, S., and H.-C. Nataf (1992), Further evidence for the 'Lay discontinuity' beneath northern Siberia and the North Atlantic from short-period P-waves recorded in France, *Phys. Earth Planet. Inter.*, *72*, 264–275.

Hutko, A. R., T. Lay, E. J. Garnero, and J. Revenaugh (2006), Seismic detection of folded, subducted lithosphere at the core-mantle boundary, *Nature*, *441*, 333–336, doi:10.1038/nature04757.

Jahnke, G., M. S. Thorne, A. Cochard, and H. Igel (2008), Global SH-wave propagation using a parallel axisymmetric spherical finite-difference scheme: Application to whole mantle scattering, *Geophys. J. Int.*, doi:10.1111/j.1365-246X.2008.03744.x.

Kawai, K., and R. J. Geller (2010), Waveform inversion for localized seismic structure and an application to D″ structure beneath the Pacific, *J. Geophys. Res.*, *115*, B01305, doi:10.1029/2009JB006503.

Kawai, K., N. Takeuchi, R. J. Geller, and N. Fuji (2007), Possible evidence for a double crossing phase transition in D″ beneath Central America from inversion of seismic waveforms, *Geophys. Res. Lett.*, *34*, L09314, doi:10.1029/2007GL029642.

Kendall, J.-M., and C. Nangini (1996), Lateral variations in D″ below the Caribbean, *Geophys. Res. Lett.*, *23*(4), 399–402, doi:10.1029/95GL02659.

Kendall, J.-M., and P. M. Shearer (1994), Lateral variations in D″ thickness from long-period shear wave data, *J. Geophys. Res.*, *99*(B6), 11,575–11,590, doi:10.1029/94JB00236.

Kito, T., S. Rost, C. Thomas, and E. J. Garnero (2007), New insights into the P- and S-wave velocity structure of the D″ discontinuity beneath the Cocos plate, *Geophys. J. Int.*, *169*, 631–645, doi:10.1111/j.1365-246X.2007.03350.x.

Krüger, F., M. Weber, F. Scherbaum, and J. Schlittenhardt (1993), Double beam analysis of anomalies in the core-mantle boundary region, *Geophys. Res. Lett.*, *20*(14), 1475–1478, doi:10.1029/93GL01311.

Lay, T. (2008), Sharpness of the D″ discontinuity beneath the Cocos Plate: Implications for the perovskite to post-perovskite phase transition, *Geophys. Res. Lett.*, *35*, L03304, doi:10.1029/2007GL032465.

Lay, T., and D. V. Helmberger (1983a), A lower mantle S-wave triplication and the shear velocity structure of D″, *Geophys. J. Roy. Astron. Soc.*, *75*, 799–838.

Lay, T., and D. V. Helmberger (1983b), The shear-wave velocity gradient at the base of the mantle, *J. Geophys. Res.*, *88*(B10), 8160–8170, doi:10.1029/JB088iB10p08160.

Lay, T., and E. J. Garnero (2011), Deep mantle seismic modeling and imaging, *Annu. Rev. Earth Planet. Sci.*, *39*, 91–123, doi:10.1146/annurev-earth-040610-133354.
Lay, T., E. J. Garnero, and S. A. Russell (2004), Lateral variation of the D″ discontinuity beneath the Cocos Plate, *Geophys. Res. Lett.*, *31*, L15612, doi:10.1029/2004GL020300.
Lay, T., J. W. Hernlund, E. J. Garnero, and M. S. Thorne (2006), A post-perovskite lens and D″ heat flux beneath the Central Pacific, *Science*, *314*, 1272–1276.
Lithgow-Bertelloni, C., and M. A. Richards (1998), The dynamics of Cenozoic and Mesozoic plate motions, *Rev. Geophys.*, *36*(1), 27–78, doi:10.1029/97RG02282.
Ma, P., P. Wang, L. Tenorio, M. V. de Hoop, and R. D. van der Hilst (2007), Imaging of structure at and near the core-mantle boundary using a generalized radon transform: 2. Statistical inference of singularities, *J. Geophys. Res.*, *112*, B08303, doi:10.1029/2006JB004513.
Matzel, E., M. K. Sen, and S. P. Grand (1996), Evidence for anisotropy in the deep mantle beneath Alaska, *Geophys. Res. Lett.*, *23*(18), 2417–2420, doi:10.1029/96GL02186.
Maupin, V., E. J. Garnero, T. Lay, and M. J. Fouch (2005), Azimuthal anisotropy in the D″ layer beneath the Caribbean, *J. Geophys. Res.*, *110*, B08301, doi:10.1029/2004JB003506.
Miyagi, L., W. Kanitpanyacharoen, P. Kaercher, K. K. M. Lee, and H.-R. Wenk (2010), Slip systems in $MgSiO_3$ post-perovskite: Implications for D″ anisotropy, *Science*, *329*, 1639–1641, doi:10.1126/science.1192465.
Murakami, M., K. Hirose, K. Kawamura, N. Sata, and Y. Ohishi (2004), Post-perovskite phase transition in $MgSiO_3$, *Science*, *304*, 855–858, doi:10.1126/science.1095932.
Oganov, A. R., and S. Ono (2004), Theoretical and experimental evidence for a post-perovskite phase of $MgSiO_3$ in Earth's D″ layer, *Nature*, *430*, 445–448.
Ohta, K., K. Hirose, T. Lay, N. Sata, and Y. Ohishi (2008), Phase transitions in pyrolite and MORB at lowermost mantle conditions: Implications for a MORB-rich pile above the core-mantle boundary, *Earth Planet. Sci. Lett.*, *267*, 107–117.
Poli, P., C. Thomas, M. Campillo, and H. A. Pedersen (2015), Imaging the D″ reflector with noise correlations, *Geophys. Res. Lett.*, *42*, 60–65, doi:10.1002/2014GL062198.
Rokosky, J. M., T. Lay, E. J. Garnero, and S. A. Russell (2004), High-resolution investigation of shear wave anisotropy in D″ beneath the Cocos Plate, *Geophys. Res. Lett.*, *31*, L07605, doi:10.1029/2003GL018902.
Rost, S., and C. Thomas (2009), Improving seismic resolution through array processing techniques, *Surv. Geophys.*, *30*, 271–299, doi:10.1007/s10712-009-9070-6.
Shang, X., S.-H. Shim, M. V. De Hoop, and R. D. Van der Hilst (2014), Multiple seismic reflectors in Earth's lowermost mantle, *Proc. Natl. Acad. Sci. U.S.A.*, doi:10.1073/pnas.1312647111.
Shim, S.-H., T. S. Duffy, R. Jeanloz, and G. Shen (2004), Stability and crystal structure of $MgSiO_3$ perovskite to the core-mantle boundary, *Geophys. Res. Lett.*, *31*, L10603, doi:10.1029/2004GL019639.
Sigloch, K., and M. G. Mihalynuk (2013), Intra-oceanic subduction shaped the assembly of Cordilleran North America, *Nature*, *496*, 50–56, doi:10.1038/nature12019.
Sun, D., and D. V. Helmberger (2008), Lower mantle tomography and phase change mapping, *J. Geophys. Res.*, *113*, B10305, doi:10.1029/2007JB005289.
Sun, D., T.-R. A. Song, and D. V. Helmberger (2006), Complexity of D″ in the presence of slab-debris and phase changes, *Geophys. Res. Lett.*, *33*, L12S07, doi:10.1029/2005GL025384.
Thomas, C., E. J. Garnero, and T. Lay (2004), High-resolution imaging of lowermost mantle structure under the Cocos plate, *J. Geophys. Res.*, *109*, B08307, doi:10.1029/2004JB003013.
Thomas, C., J. Wookey, J. Brodholt, and T. Fieseler (2011), Anisotropy as a cause for polarity reversals of D″ reflections, *Earth Planet. Sci. Lett.*, *307*, 369–376, doi:10.1016/j.epsl.2011.05.011.
Thorne, M. S., T. Lay, E. J. Garnero, G. Jahnke, and H. Igel (2007), Seismic imaging of the laterally varying D″ region beneath the Cocos Plate, *Geophys. J. Int.*, *170*, 635–648, doi:10.1111/j.1365-246X.2006.03279.x.
Thorne, M. S., Y. Zhang, and J. Ritsema (2013), Evaluation of 1-D and 3-D seismic models of the Pacific lower mantle with S, SKS, and SKKS traveltimes and amplitudes, *J. Geophys. Res. Solid Earth*, *118*, 985–995, doi:10.1002/jgrb.50054.
van der Hilst, R. D., M. V. de Hoop, P. Wang, S.-H. Shim, P. Ma, and L. Tenorio (2007), Seismostratigraphy and thermal structure of Earth's core-mantle boundary region, *Science*, *315*(5820), 1813–1817, doi:10.1126/science.1137867.
Vidale, J. E., and H. M. Benz (1993), Seismologial mapping of fine structure near the base of the Earth's mantle, *Nature*, *361*, 529–532.
Wang, P., M. V. de Hoop, R. D. van der Hilst, P. Ma, and L. Tenorio (2006), Imaging of structure at and near the core mantle boundary using a generalized radon transform: 1. Construction of image gathers, *J. Geophys. Res.*, *111*, B12304, doi:10.1029/2005JB004241.
Wang, P., M. V. de Hoop, and R. D. van der Hilst (2008), Imaging the lowermost mantle (D″) and the core-mantle boundary with SKKS coda waves, *Geophys. J. Int.*, *175*, 103–115, doi:10.1111/j.1365-246X.2008.03861.x.
Weber, M. (1993), P- and S-wave reflections from anomalies in the lowermost mantle, *Geophys. J. Int.*, *115*, 183–210.
Weber, M., and J. P. Davis (1990), Evidence of a laterally variable lower mantle structure from P- and S-waves, *Geophys. J. Int.*, *102*, 231–255.
Wenk, H.-R., S. Cottaar, C. N. Tomé, A. McNamara, and B. Romanowicz (2011), Deformation in the lowermost mantle: From polycrystal plasticity to seismic anisotropy, *Earth Planet. Sci. Lett.*, *306*, 33–45, doi:10.1016/j.epsl.2011.03.021.
Wessel, P., and W. H. F. Smith (1998), New, improved version of generic mapping tools released, *Eos Trans. AGU*, *79*(47), 579–579.
Wysession, M. E., T. Lay, J. Revenaugh, Q. Williams, E. J. Garnero, R. Jeanloz, and L. H. Kellogg (1998), The D″ discontinuity and its implications, in *The Core-Mantle Boundary Region*, edited by M. Gurnis et al., pp. 273–297, AGU, Washington, D. C.
Yamada, A., and I. Nakanishi (1998), Short-wavelength lateral variation of a D″ P-wave reflector beneath the southwestern Pacific, *Geophys. Res. Lett.*, *25*(24), 4545–4548, doi:10.1029/1998GL900188.
Yamazaki, D., T. Kato, H. Yurimoto, E. Ohtani, and M. Toriumi (2000), Silicon self-diffusion in $MgSiO_3$ perovskite at 25 GPa, *Phys. Earth Planet. Inter.*, *119*, 299–309.
Yao, Y., S. Whittaker, and M. S. Thorne (2015), D″ discontinuity structure beneath the North Atlantic from *Scd* observations, *Geophys. Res. Lett.*, *42*, 1–9, doi:10.1002/2015GL063989.
Young, C. J., and T. Lay (1987), Evidence for a shear velocity discontinuity in the lower mantle beneath India and the Indian Ocean, *Phys. Earth Planet. Inter.*, *49*, 37–53.
Young, C. J., and T. Lay (1990), Multiple phase analysis of the shear velocity structure in the D″ region beneath Alaska, *J. Geophys. Res.*, *95*(B11), 17,385–17,402, doi:10.1029/JB095iB11p17385.
Zhang, L., et al. (2014), Disproportionation of $(Mg,Fe)SiO_3$ perovskite in Earth"s deep lower mantle, *Science*, *344*, 877–882, doi:10.1126/science.1250274.